Supplemental Material

Organic carbon, sea level and carbonate weathering controls on marine carbon isotope perturbations across the Hirnantian glaciation

Figure S8. Sea level, Ca contents and carbon isotope comparison among the Monitor Range, Anticosti, Wanhe, and Shuanghe sections.

Table S1. Complied global sites

Table S2. Compiled Carbon Isotope in South China

Table S3 Integrated geochemical dataset in this study

References Cited

Text S1: Expanded geological setting

South China was situated at a low latitude during the Ordovician-Silurian (O/S) transition (Fig. S1) and consisted of the Yangtze Block to the northwest and the Cathaysia Block to the southeast (Lin et al., 2024). The northern margins of the South China Block were flooded by the tropical, epicontinental Yangtze Shelf Sea, which deepened toward the north and interconnected with the Panthalassa Ocean (Fig. 2 in main text). Upper Ordovician to lower Silurian strata in the Yangtze region comprise the basal Pagoda and Linhsiang limestones, representing early-mid Katian carbonate platform environments (Zhan et al., 2016; Zhang et al., 2023); overlying carbonaceous shales of the Wufeng Formation in deep-water shelf areas, and argillaceous limestones and interbedded calcareous shales of the Daduhe Formation deposited in shallow-water proximal shelf areas, representing regional sea-level rise and increased terrestrial inputs due to the northward progression of the Kwangsian Orogeny (Chen et al., 2014); the Hirnantian Kuanyinchiao Bed (KB), consisting of calcareous mudstones with carbonate concretions and abundant shelly fossils of the cool-water *Hirnantia*

fauna (e.g., brachiopods, trilobites, corals and gastropods) (Rong et al., 2020). This flourished during the maximum glacio-eustatic sea-level fall and disappeared abruptly with the end of the Hirnantian glaciation. The succeeding graptolitic shale of the Lungmachi Formation deposited during post-glacial marine transgression and oceanic euxinia from the latest Hirnantian to Rhuddanian (Zou et al., 2018). In the Yichang and Central Guizhou uplifts, the Lungmachi Shale directly overlies the Linhsiang Limestone, reflecting a Late Ordovician to early Silurian depositional hiatus, and exposure and erosion of the Late Ordovician carbonates during the maximum Hirnantian glaciation (Chen et al., 2018; Wang et al., 2013).

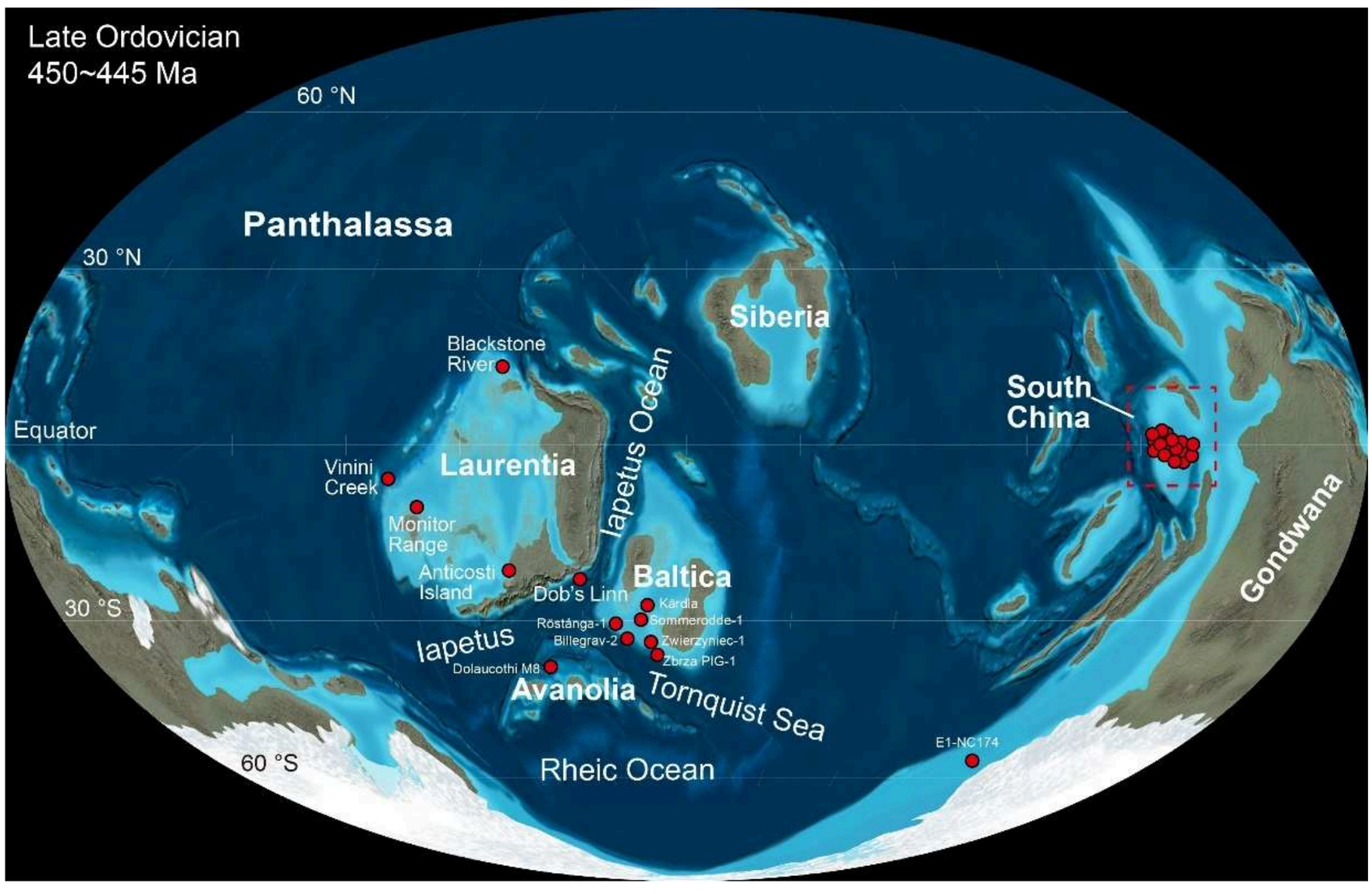

Figure S1. Late Ordovician (450~445 Ma) paleogeography showing the approximate locations of compilated sections and cores (colored dots). The base map is adapted with permission from Ron Blakey, © Colorado Plateau Geosystems Inc.

In this study, we obtained samples from four sections across the Yangtze Shelf (Fig. 2 in main text): the Wanhe section (103.4762°E, 27.7552°N), Shuanghe section (104.8842°E, 28.3847°N), Mingtongchang section (108.5461°E, 31.7697°N) and Liziping section (109.8689°E, 31.5686°N). We also compiled Ca/Al, calcite, total organic carbon (TOC) and carbon isotope data from 13 globally-distributed locations (Achab et al., 2011; Ahm et al., 2017; Bergström et al., 2016; Challands, 2008; Hammarlund et al., 2012; Hammarlund et al., 2019; Hounslow et al., 2021; Jones et al., 2016; LaPorte et al., 2009; Sánchez-Roda et al., 2024; Smolarek-Lach et al., 2019; Stockey et al., 2020; Sullivan et al., 2018; Underwood et al., 1997; Young et al., 2020; Young et al., 2010) (Fig. S1; Table S1) and 45 cores and sections in South China (Cao et al., 2023; Chen, 2018; Dong et al., 2022; Fan et al., 2009; He, 2020; Hu et al., 2021; Hu et al., 2024; Li, 2019; Li et al., 2019a; Li et al., 2021a; Li et al., 2024; Li et al., 2019b; Li et al., 2019c; Li et al., 2021c; Liu, 2017; Liu et al., 2022; Liu et al., 2016; Lu et al., 2021; Lu et al., 2022; Men et al., 2022; Qiu et al., 2020; Qiu et al., 2022a; Qiu et al., 2022b; Shen et al., 2019; Shi, 2021; Sun, 2018; Wang et al., 2021; Wang et al., 2022; Xi et al., 2021; Xiao et al., 2021; Yan et al., 2009; Yan et al., 2019; Zhang et al., 2022; Zhang et al., 2009; Zhang et al., 2021; Zhou et al., 2017; Zou et al., 2018). (Fig. S2; Table S2).

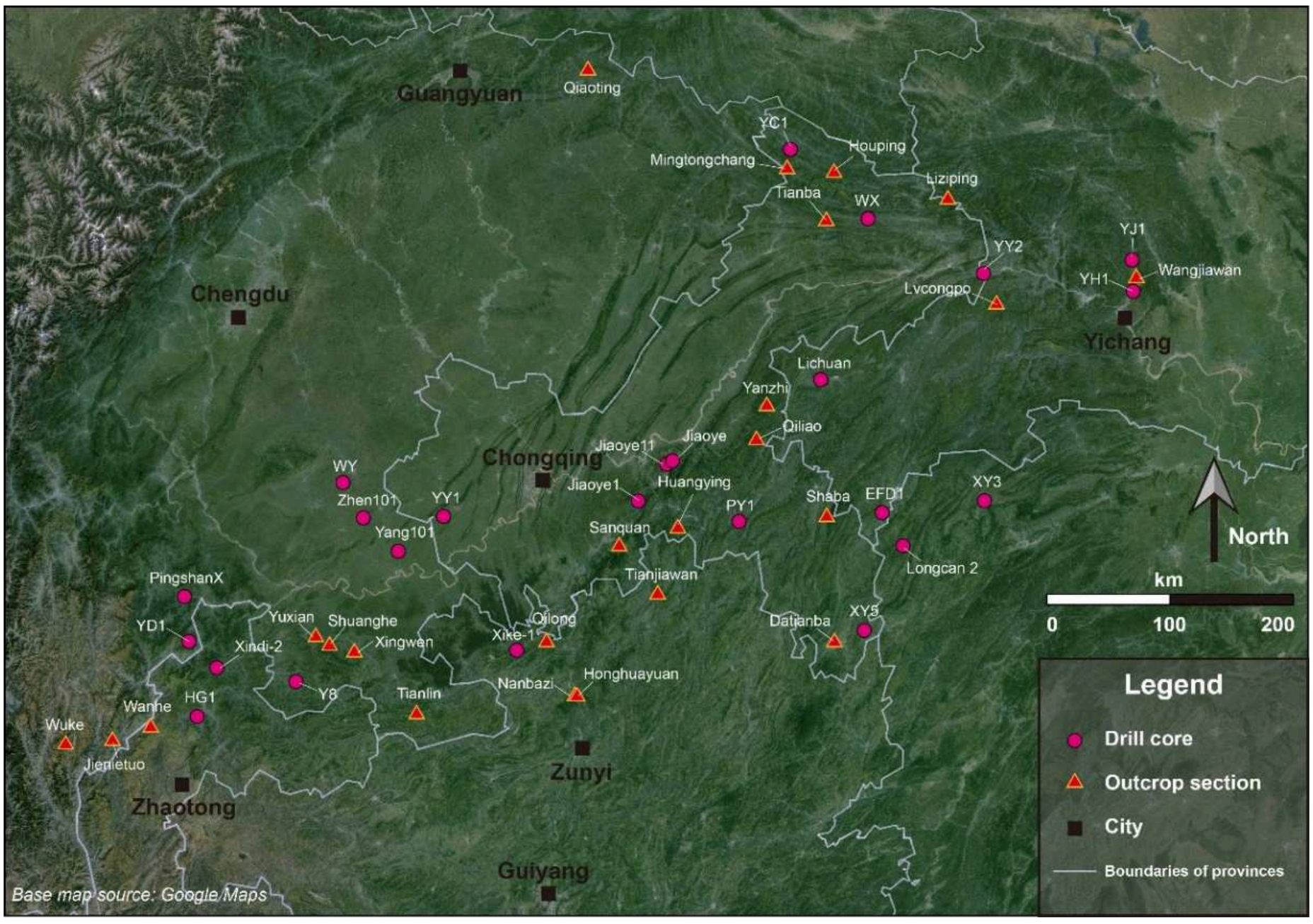

Figure S2. Locations of all sections and cores used for the TOC and $\delta^{13}C$ compilation. The base map is taken from *Google Maps*.

The Wanhe section was situated in a nearshore shallow-water area of the Yangtze Shelf Sea during the Late Ordovician. The basal part of this section consists of medium-to thick-bedded nodular limestones of the Pagoda (or Baota) Formation (0–19.8 m), representing a middle Sandbian– early Katian carbonate platform environment with a relatively stable water depth and tectonic setting (Zhan et al., 2016). Above the Pagoda Formation is the thin-bedded, nodular argillaceous limestone of the Linhsiang (or Linxiang) Formation (19.8–29.8m), reflecting sea-level fall (Zhan and Jin, 2007). The overlying Daduhe Formation can be divided into two members: the lower member (29.8– 42.9 m) consists of thin-bedded argillaceous

limestone interbedded with calcareous mudstone, while the upper member (42.9–51.9 m) comprises calcareous mudstone/shale intercalated with argillaceous limestone. The topmost part of the Daduhe Formation is the Kuanyinchiao Bed (51.9– 58.6 m), which consists of lenticular argillaceous limestone and calcareous mudstone, and is rich in shelly fossils (Fig. S2). The Lungmachi (or Longmaxi) Formation conformably overlies the Kuanyinchia Bed and consists of black graptolitic shale in the lower part (52. 6 m–58.6 m), grading up into silty shale or mudstone in the mid-upper part (58.6–81 m).

During the late Katian, the Shuanghe section was consistently situated in a deep inner-shelf setting. The Wufeng Formation in this section is composed of black graptolitic shale and calcareous mudstone, with a thickness of 10 m (Zou et al., 2018). The Kuanyinchiao Bed is about 60 cm thick and mainly comprises calcareous mudstone and lenticular shelly mudstone. The Lungmachi Formation comprises black graptolitic shale with a thickness of over 10 m.

The Mingtongchang and Liziping sections accumulated in a deep-water outer shelf environment during the O/S transition. (Li et al., 2021b; Xiao et al., 2022). Sedimentary successions and lithofacies in the two sections can be correlated with the Shuanghe and Wangjiawan sections (Chen et al., 2006). Notably, the Wufeng Formation is relatively thin (about 2 m), and the Kuanyinchiao Bed is composed of ~ 2 m of black calcareous siltstone at the Liziping section. The Lungmachi Formation comprises black siliciclastic shale with abundant graptolites, with a thickness of over

20 m in the two sections.

Text S2: Hirnantian carbonate-rich deposits—the Kuanyinchiao Bed

The Kuanyinchiao Bed, deposited between the Wufeng and Lungmachi shales, is characterized by high carbonate concentrations and abundant shelly fossils of the well-known, cool-water *Hirnantia* fauna, which includes brachiopods, trilobites, corals and gastropods (Rong et al., 2020) (Fig. S3). The Kuanyinchiao Bed is widely distributed on the Yangtze Shelf and records a dramatic eustatic sea-level drop (at least 80 m; (Brenchley et al., 2006) during the peak Hirnantian glaciation (Zhan and Jin, 2007). The thickest and most complete lithological sequence of the Kuanyinchiao Bed is found at the Honghuayuan section of Tongzi, northern Guizhou Province, where it reaches a thickness of over 5 m and consists of multiple layers of grey, mid-bedded argillaceous limestone (Fig. S3A-B) intercalated with graptolitic shales. In the Wanhe section, this formation is composed of lenticular argillaceous limestone and calcareous mudstone with a thickness of 0.7 m (Fig. S3C-D).

In deep-water environments, the Kuanyinchiao Bed is generally less than 1 m thick and consists of lenticular, shelly argillaceous limestone and calcareous mudstone (Zhang et al., 2016), such as a 0.6 m thick lenticular shelly limestone at Shuanghe (inner shelf; Fig. S3E-G), a 0.27 m thick lenticular shelly limestone at Huangying (mid-shelf; Fig. S3H-I), and a 0.3 m thick shelly calcareous mudstone at Qiliao (mid-shelf; Fig. S3J). In outer-shelf regions, there is an increase in siliciclastic content, but this formation remains rich in carbonate. For instance, at the Liziping section, the

Kuanyinchiao Bed is distinguished by ~ 2 m of calcareous siltstone (Fig. S3K). Notably, Hirnantian carbonate-rich deposition is widespread throughout other continents (Jones et al., 2011; LaPorte et al., 2009; Melchin and Holmden, 2006). Even in deep basin settings, significant carbonate enrichments (indicated by elevated $CaCO_3$ and Ca/Al values) occur in the Hirnantian intervals, suggesting a global-scale carbonate burial event.

Figure S3. Representative field photographs of the Kuanyinchiao Bed (KB) throughout the Yangtze Shelf. A: The boundary between the Lungmachi Formation

and the Kuanyinchiao Bed at the Honghuayuan section, Tongzi, Guizhou. B: Enlargement of mid-bedded argillaceous limestone and calcareous siltstone within the Kuanyinchiao Bed in Fig. S3A. C: Lenticular argillaceous limestone and calcareous mudstone of the Kuanyinchiao Bed at the Wanhe section, Zhaotong, Yunnan. D: Enlargement of shelly argillaceous limestone in Fig. S3C showing brachiopods (yellow dashed circles). E: Black lenticular shelly limestone at the Shuanghe section, Changning, Sichuan. F– G: Enlargement of shelly limestone in Fig. S3E showing brachiopods (the yellow dashed circle). H: The O-S transition succession at the Huangying section, Wulong, Chongqing. I: Enlargement of shelly limestone seen in Fig. S3H showing *Hirnantia* that have been pyritized. J: Calcareous mudstone of the Kuanyinchiao Bed at the mid-shelf Qiliao section, Shizhu, Chongqing. K: Calcareous siltstone of the Kuanyinchiao Bed at the out-shelf Liziping section, Zhuxi, Hubei.

Text S3: Materials and methods

A total of 200 outcrop samples were collected from the four sections in the Yangtze region, South China, including 108 samples from the Wanhe section, 43 samples from the Shuanghe section, 25 samples from the Mingtongchang section, and 24 samples from the Liziping section. Before geochemical analysis, the fresh samples were carefully trimmed to remove weathered surfaces, visible veins and pyrite nodules. The remaining sample was then powdered to approximately 200 mesh using an agate mill. All samples were analyzed for major elements and total organic carbon (TOC) content at the Key Laboratory of Petroleum Resources of the Northwest Institute of

Eco-Environment and Resources, Chinese Academy of Sciences, Lanzhou, China. Additionally, 157 samples from the Wanhe, Mingtongchang and Liziping sections were analyzed for organic carbon isotopes, and 84 samples from the Wanhe (41) and Shuanghe (43) sections were analyzed for carbonate carbon isotopes, Ca isotopes and trace element (Sr, U) concentrations in carbonate minerals at the State Key Laboratory of Geological Processes and Mineral Resources, China University of Geosciences, Wuhan, China. All data are shown in Table S3.

Organic carbon contents and isotopes

Prior to analysis, ~0.1 g of dried sample powder was decarbonated via two sequential dissolutions with 4 M HCl at room temperature. Samples were then washed with deionized water to remove all remaining acid and dried at 50℃. TOC contents were measured using a CS-902C High Frequency Infrared Carbon Sulfur Analyzer. The analytical reproducibility was better than ±0.1% based on duplicate analyses. Organic carbon isotopes ($\delta^{13}C_{org}$) were analyzed using a Finnigan MAT253 Mass Spectrometer and reported in standard δ-notation relative to the Vienna Peedee Belmnite (VPDB) standard. The analytical reproducibility of $\delta^{13}C_{org}$ was better than ± 0.1‰.

Carbonate carbon isotope analysis

About 100 mg of sample powder was weighed into a 10 mL Na glass vial, and then sealed by a butyl rubber septum. After flushing with helium gas, the sample was

reacted with 100% phosphoric acid at 72°C to release CO_2. The carbonate carbon isotope ($\delta^{13}C_{carb}$) compositions of the released CO_2 were then measured with a MAT253 Mass Spectrometer and isotope data was calculated as permil (‰) relative to the VPDB standard. The analytical reproducibility was better than ±0.1‰.

Elemental analysis of whole-rock samples

Bulk major element analyses were measured using a PANalytical Sequential X-ray Fluorescence (XRF) spectrometer. Prior to analysis, powdered samples were dried at 105°C. Approximately 4 g of dried sample powder was weighed into a mold with boric acid lining the edges and bottom. The powdered samples were pressed into a pellet with an inner diameter of 32 mm using a ZHY-401A press machine at a pressure of 30 tons. The raw data were analyzed using SuperQ (Version 5.0) Software. The analytical precision for all major elements was maintained at better than ±3%.

For bulk trace element analysis, ~50 mg of sample powder was weighed into Teflon beakers. Sequentially, 1.50 mL of 68% HNO_3, 1.5 mL of HF, and 0.01 mL of $HClO_4$ were added to the Teflon beakers. Afterwards, the Teflon beakers were placed on a hotplate at 140°C. Dissolved samples were evaporated to dryness,then re-dissolved in 1.50 mL HNO_3 and 1.50 mL HF. Then the capped Teflon beakers were placed into an oven at 195°C for over 48 h. Dissolved samples were evaporated to dryness, and then 3 mL HNO_3 was added. Re-dissolved samples were evaporated to dryness, and then 3 mL 50% HNO_3 was added and the beakers placed into an oven at 150°C for 24 h. The dissolved samples were transferred into 100 mL tubes, and Rh

internal standard solution was added. Deionized water was added into the tube to 100 g, ensuring the concentration of Rh in the solution was 50 mg/mL. The final solutions were analyzed using an inductively coupled plasma mass spectrometer (ICP-MS Agilent 7700e).

Elemental analysis of carbonate minerals

For the analysis of trace elements in carbonates, about 200 mg of sample powder was individually weighed into centrifuge tubes, and 2 mL of deionized water was added. After 10 mins vibration, the samples were centrifuged at 4000 rpm for 10 mins and all supernatant was removed. The deionized water washing procedure was repeated. After washing, the samples were dried and finely re-ground. Next, about 50 mg of the dried sample powder was weighed into a new centrifuge tube, and 0.25 mL of acetic acid (0.86 M) was added. The samples were sonicated for 30 minutes, then allowed to react at room temperature for 24 h. Subsequently, the samples were centrifuged again at 4000 rpm for 10 mins, and the supernatant was removed. To ensure complete removal of absorbed Ca, the acetic acid washing procedure was repeated. Afterwards, the samples were then re-dried and re-ground. Subsequently, the samples were re-dissolved with 0.5 mL of 0.86 M acetic acid. After 30 minutes vibration, the samples were allowed to react at room temperature for 24 h. Subsequently, the samples were centrifuged again at 4000 rpm for 10 mins, and the supernatant was carefully transferred into a new Teflon vial. This final extraction with acetic acid was repeated twice for each sample, with all supernatants added into the same Teflon vial. The

resulting solution was analyzed for trace elements using an ICP-MS (Agilent 7700e).

Calcium isotope analysis of carbonate minerals

In this study, we only analyzed Ca isotope compositions of carbonate minerals, rather than whole-rock samples. The same extraction procedure for carbonate as described above for testing trace elements in carbonate rocks was applied. Therefore, the initial dissolved sample solutions used for Ca isotope measurements are identical to the final dissolved sample solutions for carbonate trace element analysis. Firstly, an aliquot containing about 40 μg of Ca was transferred into a 7 mL vial. The solution was dried and re-dissolved with 400 mL of 4 mol/L HNO_3 and then loaded on DGA extraction chromatography resin to purify. About 6 mL of 4 mol/L HNO3 was added to completely rinse off matrix elements. 3 mL of deionized water was subsequently added to quantitatively elute the Ca. The purified sample solutions were evaporated to dryness and re-dissolved with 2 mL of 0.35 mol/L HNO_3 prior to calcium isotope measurements. The final sample solutions were measured for calcium isotope ratios using a multi-collector inductively coupled plasma mass spectrometer (MC-ICP-MS; Nu Plasma 1700) operated in high-resolution mode. The Ca isotopic compositions of the samples are reported as δ-notation relative to seawater ($\delta^{44}Ca–SW$):

$$\delta^{44}Ca\ (\text{in}\ ‰) = [(^{44}Ca / {}^{40}Ca)_{sample} / (^{44}Ca / {}^{40}Ca)_{SW} - 1] \times 1000$$

Measurement uncertainty for each sample is ±0.06‰ (two-standard deviation: 2SD) and the long-term external precision of $\delta^{44}Ca$ is better than ±0.07 ‰ (2SD) (Li et al., 2018). In this study, the average $\delta^{44}Ca$ value of the SRM 915a standard relative to

seawater was 1.92 ± 0.07‰.

Age model

Each of our samples and compiled data were assigned chronometric ages using age-constrained graptolite zones (Fig. S4). The Stage boundary ages and durations of each graptolite zone are derived from the latest International Chronostratigraphic Chart (v2023/09) and the 2012 Geologic Time Scale (Cooper et al., 2012). For a few global shallow-water sections without graptolite zones, we used well-established conodont or chitinozoan zones. Global correlation among graptolite, conodont and chitinozoan biozones was based on the framework of Goldman et al. (2023). Linear ages were constructed assuming a constant sedimentation rate within the age-controlled graptolite zone.

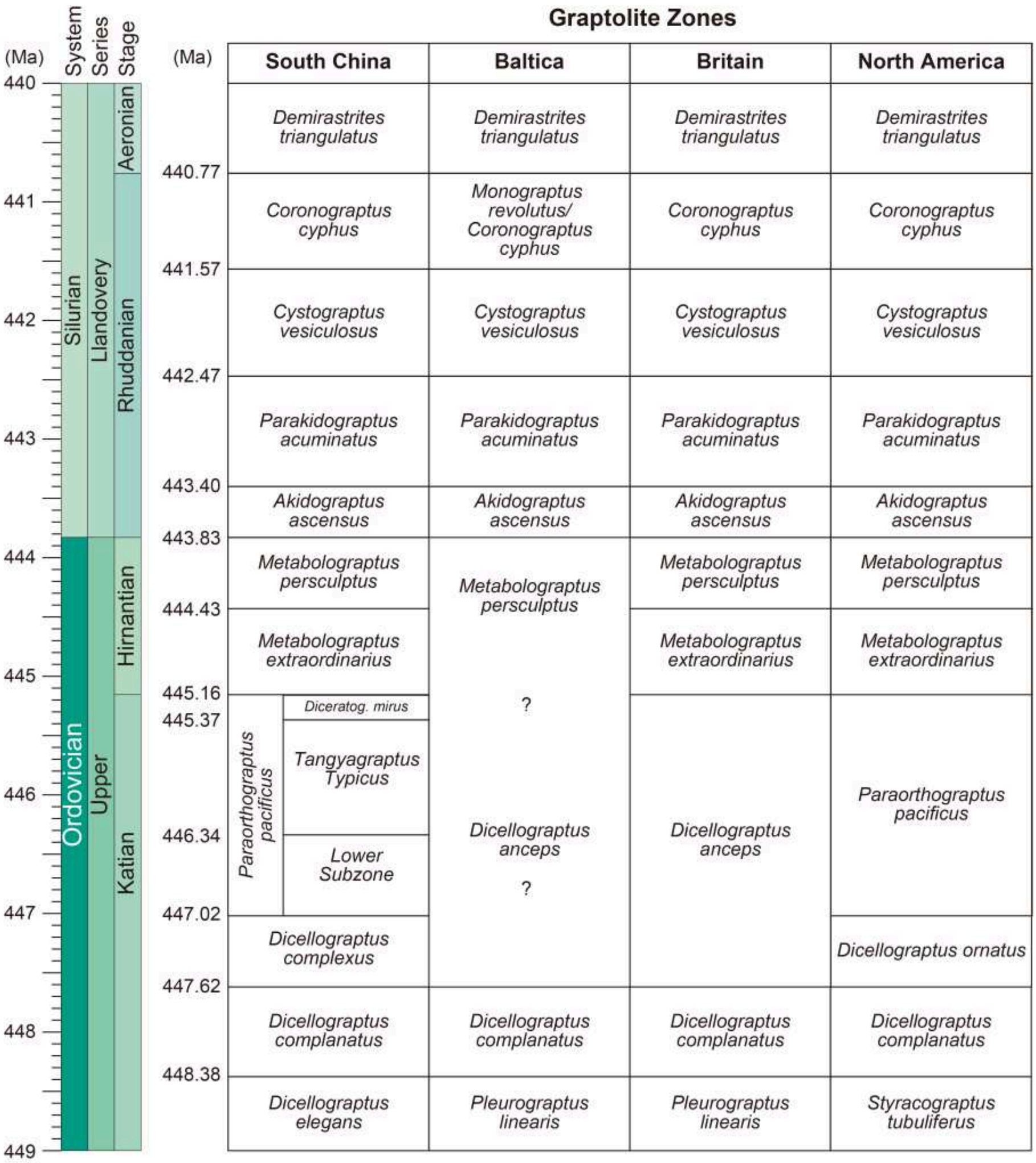

Figure S4. Global correlation chart of graptolite zonation and referenced ages from the Upper Ordovician to Lower Silurian (Chen et al., 2000; Chen et al., 2006; Cooper et al., 2012; Goldman et al., 2023).

Processing of compiled $\delta^{13}C_{org}$ data

A total of about 2100 data points from 42 drill cores and outcrop sections were used to map lateral variability in $\delta^{13}C_{org}$ values on the Yangtze Shelf across the Hirnantian

glaciation. According to our age framework, we assigned an interpreted age to all data points. To reduce the influence from outliers, we extracted six $\delta^{13}C_{org}$ values with 1 Ma intervals between 447.5Ma and 442.5Ma from the 10% LOWESS (locally weighted scatterplot smoothing) fitted $\delta^{13}C_{org}$ curves (Fig. S5) for each section. The LOWESS regression was performed using Matlab Software. Maps of $\delta^{13}C_{org}$ were created using Surfer software, and a kriging method was applied for map grids.

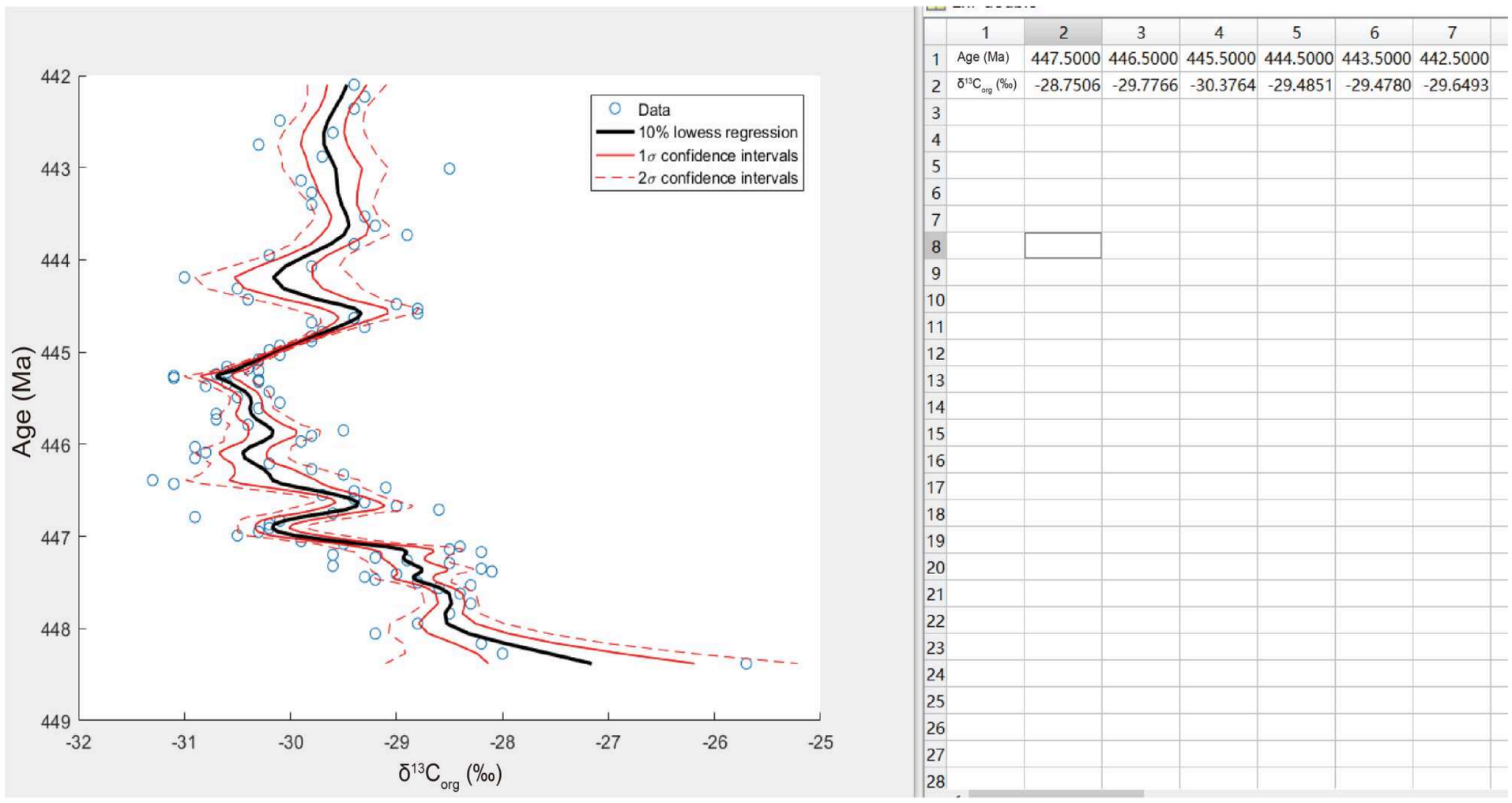

	1	2	3	4	5	6	7
1	Age (Ma)	447.5000	446.5000	445.5000	444.5000	443.5000	442.5000
2	$\delta^{13}C_{org}$ (‰)	-28.7506	-29.7766	-30.3764	-29.4851	-29.4780	-29.6493

Figure S5. Example of six extracted $\delta^{13}C_{org}$ values from the 10% LOWESS fitted curve in the Wanhe section.

Text S4: Framework for calcium isotope and diagenesis interpretations

Carbonate minerals preferentially sequester light Ca isotopes from seawater, exhibiting a $\delta^{44}Ca$ offset of ~-1.5‰ for aragonite and ~-0.9‰ for calcite compared to

contemporaneous seawater (Gussone et al., 2020). However, post-depositional diagenetic processes (in particular, early marine diagenesis) can alter and reset original $\delta^{13}C$ and $\delta^{44}Ca$ signals recorded in carbonate sediments (Fantle and Higgins, 2014; Higgins et al., 2018). Paired measurement of $\delta^{44}Ca$, Sr/Ca and U/Ca ratios is a potential approach to constrain the extent and style of early marine diagenetic alteration in carbonate rocks (Ahm et al., 2018; Higgins et al., 2018). Shallow-water carbonate sediments are often associated with fluid-buffered alteration, characterized by extensive exchange between porewater and seawater, resulting in isotopic equilibrium between diagenetic carbonate minerals and seawater (Hoffman and Lamothe, 2019; Holmden et al., 2024). In such open diagenetic regimes, the $\delta^{44}Ca$ values in diagenetic minerals are expected to increase to approach contemporaneous seawater compositions (~0‰ in modern seawater, ~-0.7‰ to ~-0.25‰ in the Late Ordovician seawater) (Holmden, 2009; Holmden et al., 2024), while Sr/Ca and U/Ca ratios would be lowered compared to primary aragonite or calcite (Busch et al., 2022). By contrast, the isotopic signatures of $\delta^{13}C$ and $\delta^{44}Ca$ in deep-water carbonate sediments may be preserved during early marine diagenesis due to sluggish porewater circulation (in a closed system) and the majority of the re-precipitated Ca is inherited from the precursor carbonate minerals (under sediment-buffered conditions) (Ahm et al., 2018; Hoffman and Lamothe, 2019; Holmden et al., 2024). In the cross-plots of $\delta^{44}Ca$ vs. Sr/Ca and $\delta^{44}Ca$ vs. U/Ca (Fig. S6), our mudstone/shale samples from the Shuanghe section and most shale samples from the Wanhe section plotted in or near

to the sediment buffered field, showing no apparent covariation between Sr/Ca and $\delta^{44}Ca$, or U/Ca and $\delta^{44}Ca$. The carbonate samples from the Wanhe section are closer to the seawater-buffered field, exhibiting a broadly negative covariation between Sr/Ca and $\delta^{44}Ca$, as well as U/Ca and $\delta^{44}Ca$. In addition, limestone samples have lower Sr/Ca and U/Ca values, and high $\delta^{44}Ca$ values. This is consistent with shallower sedimentary settings for carbonate rocks, which were characterized by extensive exchange between porewater and seawater, resulting in $\delta^{44}Ca$ signals of carbonate minerals increasing to seawater values, along with the loss of some Sr and U (Busch et al., 2022). We thus suggest that our shale samples deposited from the relatively deep-water settings preserve the original $\delta^{44}Ca$ signals and can be used to reconstruct local marine Ca cycling. By contrast, $\delta^{44}Ca$ signals of carbonate samples from the Wanhe section may have been altered during early marine diagenesis.

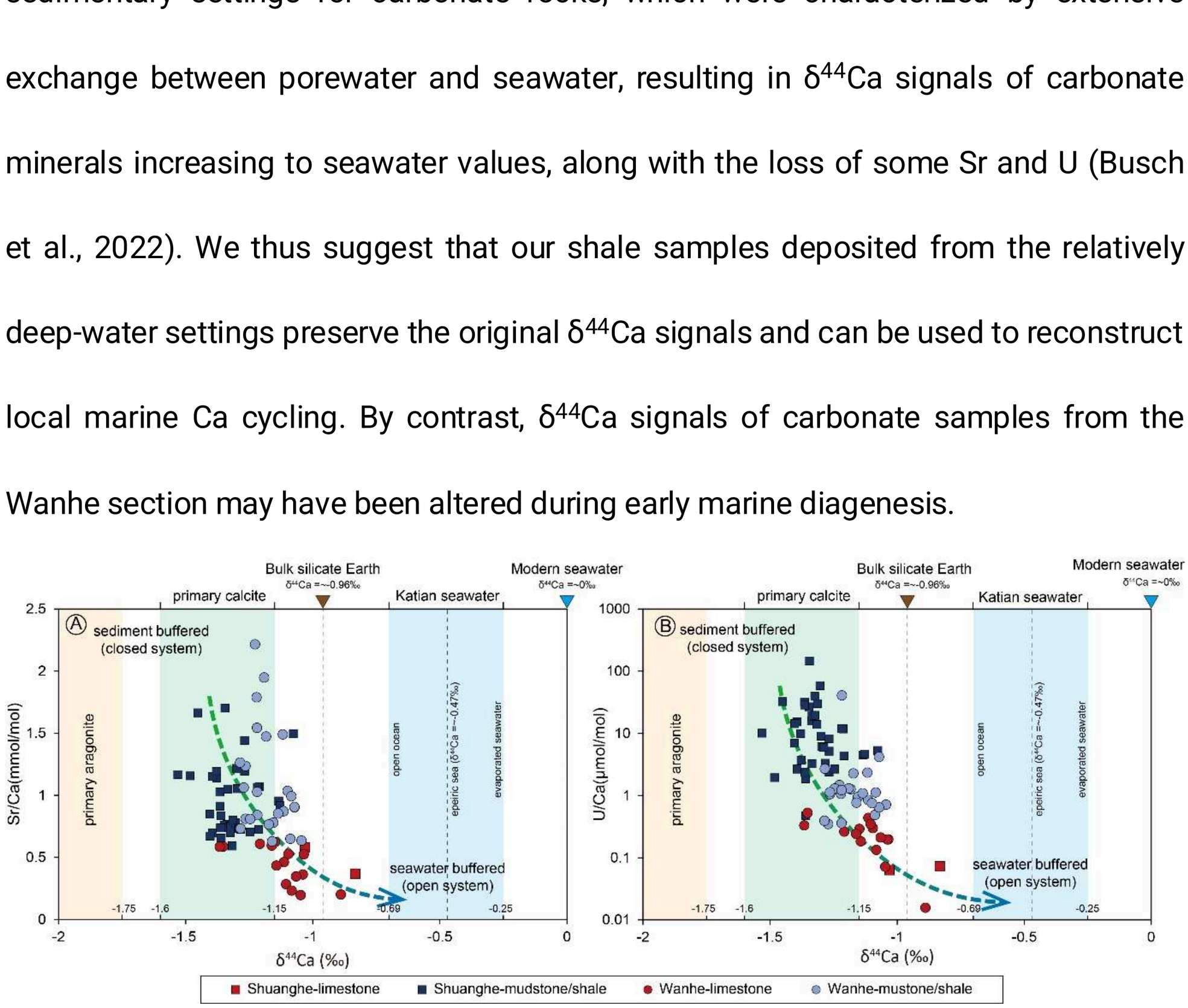

Figure S6. Cross-plots of $\delta^{44}Ca$ vs. Sr/Ca and $\delta^{44}Ca$ vs. U/Ca. The $\delta^{44}Ca$ value of bulk silicate Earth (~-0.96‰ relative to modern seawater) is from Fantle and Tipper (2014). The range of $\delta^{44}C$ values of primary calcite and aragonite are calculated based on the average fractionation factors of -0.9‰ and -1.5‰ for the two carbonate minerals,

312 respectively, (Gussone et al., 2020), as well as the estimated $\delta^{44}Ca$ ranges (~-0.7‰ to

313 ~-0.25‰) of Late Ordovician seawater from Holmden, 2009 and Holmden et al., 2024.

314

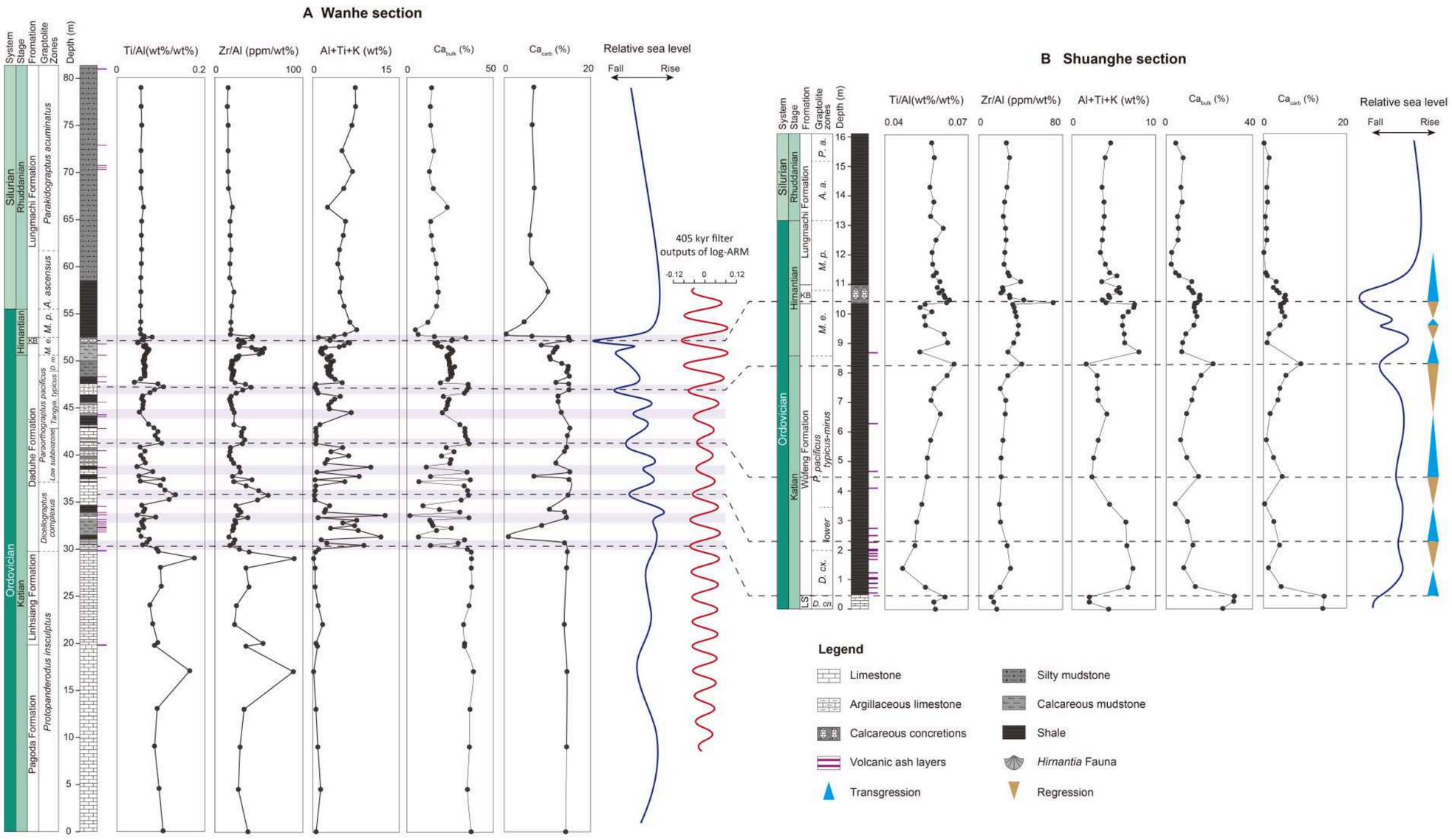

315

316 **Figure S7. Sea-level history in the Wanhe and the Shuanghe sections.** Overall, black

317 shale facies with low Ti/Al, Zr/Al, Al+K+Ti, bulk Ca (Ca_{bulk}) and carbonate Ca (Ca_{carb})

318 concentrations are interpreted to reflect rising sea-level and associated

319 carbonate-platform drowning (Fanton and Holmden, 2007; LaGrange et al., 2020; Li et

320 al., 2021a). The light-purple shaded band denotes low sea-level intervals. $\delta^{13}C_{org}$ and

321 bulk Ca data for the Shuanghe section are replotted from Zou et al. (2018). The

322 log-transformed anhysteretic remanent magnetization (ARM) profile of the Wanhe

323 section is redrawn from Zhong et al. (2020). Notably, in the Daduhe Formation of the

324 WH section, sea-level fluctuations correlate well with 405 thousand year Milankovitch

325 cycles, and can be compared with long-term transgression–regression cycles in the

326 coeval Wufeng Formation of the SH section.

327

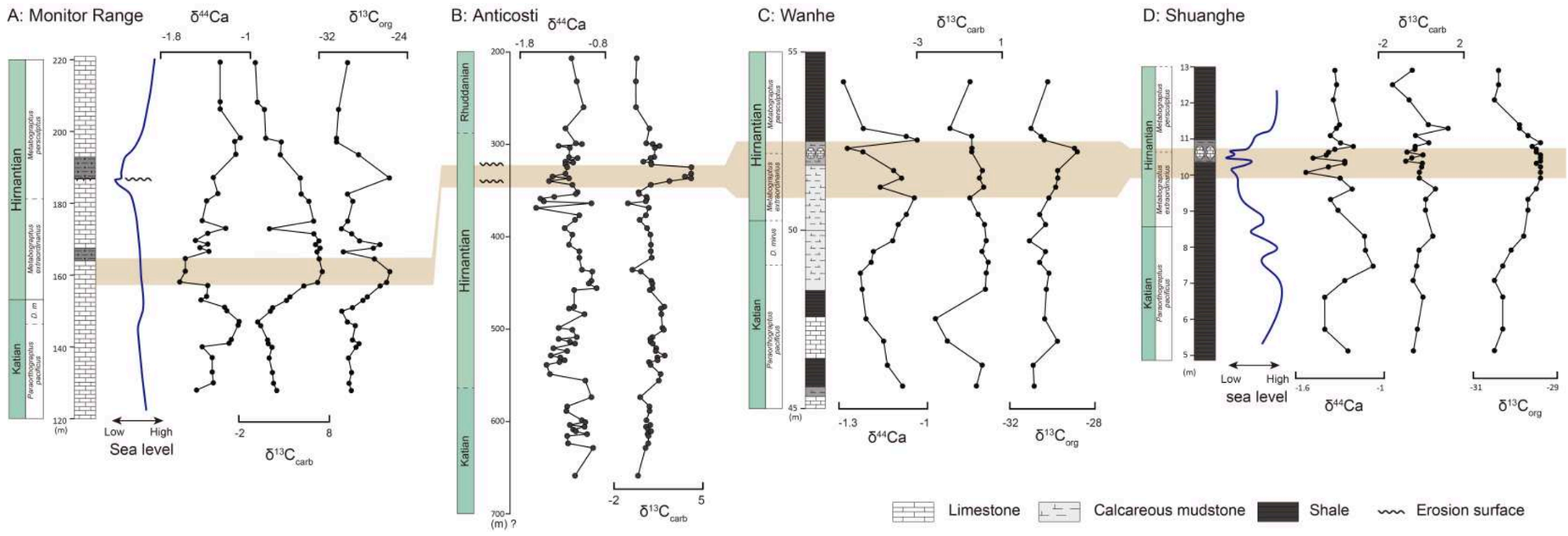

Figure S8. Sea level, Ca contents and carbon isotope comparison among the Monitor Range (A) (Holmden et al., 2012)**, Anticosti** (Jones et al., 2019) **(B), Wanhe (C), and Shuanghe (D) sections.**

REFERENCES CITED

Achab, A., Asselin, E., Desrochers, A., Riva, J. F., and Farley, C., 2011, Chitinozoan biostratigraphy of a new Upper Ordovician stratigraphic framework for Anticosti Island, Canada: GSA Bulletin, v. 123, no. 1-2, p. 186-205.

Ahm, A.-S. C., Bjerrum, C. J., Blättler, C. L., Swart, P. K., and Higgins, J. A., 2018, Quantifying early marine diagenesis in shallow-water carbonate sediments: Geochimica et Cosmochimica Acta, v. 236, p. 140-159.

Ahm, A.-S. C., Bjerrum, C. J., and Hammarlund, E. U., 2017, Disentangling the record of diagenesis, local redox conditions, and global seawater chemistry during the latest Ordovician glaciation: Earth and Planetary Science Letters, v. 459, p. 145-156.

Bergström, S. M., Eriksson, M. E., Schmitz, B., Young, S. A., and Ahlberg, P., 2016, Upper Ordovician δ13Corg chemostratigraphy, K-bentonite stratigraphy, and biostratigraphy in southern Scandinavia: A reappraisal: Palaeogeography, Palaeoclimatology, Palaeoecology, v. 454, p. 175-188.

Brenchley, P. J., Marshall, J. D., Harper, D. A. T., Buttler, C. J., and Underwood, C. J., 2006, A late Ordovician (Hirnantian) karstic surface in a submarine channel, recording glacio-eustatic sea-level changes: Meifod, central Wales: Geological Journal, v. 41, no. 1, p. 1-22.

Busch, J. F., Hodgin, E. B., Ahm, A.-S. C., Husson, J. M., Macdonald, F. A., Bergmann, K. D., Higgins, J. A., and Strauss, J. V., 2022, Global and local drivers of the

Ediacaran Shuram carbon isotope excursion: Earth and Planetary Science Letters, v. 579, p. 117368.

Cao, G., Liu, Y., Zhou, X., and Li, Y., 2023, Sedimentary Environment and Accumulation Pattern of Organic Matter in Wufeng-Longmaxi Formations in the Southwestern Sichuan,China: Journal of Earth Sciences and Environment, v. 45, no. 05, p. 1227-1245.

Challands, T. J., 2008, Geosphere and Biosphere dynamics during late Ordovician climate change: Durham University.

Chen, C., 2018, Research on paleoceanography, paleoclimate and formation mechanism of source rock during geologic transition period from Late Ordovician to early Silurian in southern Sichuan province-northern Guizhou province, South China [Doctor: China University of Geosciences (Wuhan), 155 p.

Chen, X., Chen, Q., Zhen, Y., Wang, H., Zhang, L., Zhang, J., Wang, W., and Xiao, Z., 2018, Circumjacent distribution pattern of the Lungmachian graptolitic black shale (early Silurian) on the Yichang Uplift and its peripheral region: Science China Earth Sciences, v. 61, no. 9, p. 1195-1203.

Chen, X., Fan, J., Chen, Q., Tang, L., and Hou, X., 2014, Toward a stepwise Kwangsian Orogeny: Science China Earth Sciences, v. 57, no. 3, p. 379-387.

Chen, X., Rong, J., Charles E., M., David A. T., H., Fan, J., Zhan, R., Zhang, Y., Li, R., and Wang, Y., 2000, Late Ordovician to earliest Silurian graptolite and brachiopod biozonation from the Yangtze region, South China, with a global correlation:

Geological Magazine, v. 137, no. 6, p. 623-650.

Chen, X., Rong, J., Fan, J., Zhan, R., Charles, E. M., David, A. T. H., Michael, J. M., Stan, C. F., and Wang, X., 2006, The Global Boundary Stratotype Section and Point (GSSP) for the base of the Hirnantian Stage (the uppermost of the Ordovician System): Episodes, v. 29, no. 3, p. 183-196.

Cooper, R. A., Sadler, P. M., Hammer, O., and Gradstein, F. M., 2012, Chapter 20 - The Ordovician Period, *in* Gradstein, F. M., Ogg, J. G., Schmitz, M. D., and Ogg, G. M., eds., The Geologic Time Scale: Boston, Elsevier, p. 489-523.

Dong, Z., Wang, Z., Zhang, W., Zhao, F., Du, Y., Zhu, Y., Fu, X., and Wang, C., 2022, Dynamic sulfur and carbon cycles related to microbial sulfate reduction and volcanic activity during the Hirnantian glaciation in the Upper Yangtze Basin, South China: Frontiers in Earth Science, v. 10.

Fan, J., Peng, P. a., and Melchin, M. J., 2009, Carbon isotopes and event stratigraphy near the Ordovician–Silurian boundary, Yichang, South China: Palaeogeography, Palaeoclimatology, Palaeoecology, v. 276, no. 1, p. 160-169.

Fantle, M. S., and Higgins, J., 2014, The effects of diagenesis and dolomitization on Ca and Mg isotopes in marine platform carbonates: Implications for the geochemical cycles of Ca and Mg: Geochimica et Cosmochimica Acta, v. 142, p. 458-481.

Fantle, M. S., and Tipper, E. T., 2014, Calcium isotopes in the global biogeochemical Ca cycle: Implications for development of a Ca isotope proxy: Earth-Science Reviews, v. 129, p. 148-177.

Fanton, K. C., and Holmden, C., 2007, Sea-level forcing of carbon isotope excursions in epeiric seas: implications for chemostratigraphy: Canadian Journal of Earth Sciences, v. 44, no. 6, p. 807-818.

Goldman, D., Leslie, S. A., Liang, Y., and Bergström, S. M., 2023, Ordovician biostratigraphy: index fossils, biozones and correlation: Geological Society, London, Special Publications, v. 532, no. 1, p. 31-62.

Gussone, N., Ahm, A.-S. C., Lau, K. V., and Bradbury, H. J., 2020, Calcium isotopes in deep time: Potential and limitations: Chemical Geology, v. 544, p. 119601.

Hammarlund, E. U., Dahl, T. W., Harper, D. A. T., Bond, D. P. G., Nielsen, A. T., Bjerrum, C. J., Schovsbo, N. H., Schönlaub, H. P., Zalasiewicz, J. A., and Canfield, D. E., 2012, A sulfidic driver for the end-Ordovician mass extinction: Earth and Planetary Science Letters, v. 331-332, p. 128-139.

Hammarlund, E. U., Loydell, D. K., Nielsen, A. T., and Schovsbo, N. H., 2019, Early Silurian δ13Corg excursions in the foreland basin of Baltica, both familiar and surprising: Palaeogeography, Palaeoclimatology, Palaeoecology, v. 526, p. 126-135.

He, L., 2020, Organic Matter Enrichment and Evolution of Sedimentary Environment of the Wufeng-Longmaxi Shale in Southeastern Margins of the Sichuan Basin [Doctor: Chinese Academy of Sciences.

Higgins, J. A., Blättler, C. L., Lundstrom, E. A., Santiago-Ramos, D. P., Akhtar, A. A., Crüger Ahm, A. S., Bialik, O., Holmden, C., Bradbury, H., Murray, S. T., and Swart, P.

K., 2018, Mineralogy, early marine diagenesis, and the chemistry of shallow-water carbonate sediments: Geochimica et Cosmochimica Acta, v. 220, p. 512-534.

Hoffman, P. F., and Lamothe, K. G., 2019, Seawater-buffered diagenesis, destruction of carbon isotope excursions, and the composition of DIC in Neoproterozoic oceans: Proceedings of the National Academy of Sciences, v. 116, no. 38, p. 18874-18879.

Holmden, C., 2009, Ca isotope study of Ordovician dolomite, limestone, and anhydrite in the Williston Basin: Implications for subsurface dolomitization and local Ca cycling: Chemical Geology, v. 268, no. 3, p. 180-188.

Holmden, C., Kimmig, S. R., and Nadeau, M. D., 2024, Ca isotopic gradients in epeiric marine carbonates: Diagenetic origins of and significance for Ca cycle reconstructions: Geochimica et Cosmochimica Acta.

Holmden, C., Panchuk, K., and Finney, S. C., 2012, Tightly coupled records of Ca and C isotope changes during the Hirnantian glaciation event in an epeiric sea setting: Geochimica et Cosmochimica Acta, v. 98, p. 94-106.

Hounslow, M. W., Ratcliffe, K. T., Harris, S. E., Nawrocki, J., Wójcik, K., Montgomery, P., and Woodcock, N. H., 2021, The Telychian (early Silurian) oxygenation event in northern Europe: A geochemical and magnetic perspective: Palaeogeography, Palaeoclimatology, Palaeoecology, v. 567, p. 110277.

Hu, D., Li, M., Chen, J., Luo, Q., Grasby, S. E., Zhang, T., Yuan, S., Xu, Y., Finney, S. C., Sun, L., and Shen, Y., 2021, Major volcanic eruptions linked to the Late Ordovician

mass extinction: Evidence from mercury enrichment and Hg isotopes: Global and Planetary Change, v. 196, p. 103374.

Hu, R., Tan, J., Wang, W., Song, X., Pogge von Strandmann, P. A. E., Dick, J., and Liu, C., 2024, Coupling of nitrogen biogeochemical cycling and phytoplankton community structure before and after the Late Ordovician mass extinction in South China: Chemical Geology, v. 647, p. 121933.

Jones, D. S., Brothers, R. W., Crüger Ahm, A.-S., Slater, N., Higgins, J. A., and Fike, D. A., 2019, Sea level, carbonate mineralogy, and early diagenesis controlled δ13C records in Upper Ordovician carbonates: Geology, v. 48, no. 2, p. 194-199.

Jones, D. S., Creel, R. C., and Rios, B. A., 2016, Carbon isotope stratigraphy and correlation of depositional sequences in the Upper Ordovician Ely Springs Dolostone, eastern Great Basin, USA: Palaeogeography, Palaeoclimatology, Palaeoecology, v. 458, p. 85-101.

Jones, D. S., Fike, D. A., Finnegan, S., Fischer, W. W., Schrag, D. P., and McCay, D., 2011, Terminal Ordovician carbon isotope stratigraphy and glacioeustatic sea-level change across Anticosti Island (Québec, Canada): GSA Bulletin, v. 123, no. 7-8, p. 1645-1664.

Lagrange, M.T., Konhauser, K.O., Catuneanu, O., Harris, B.S., Playter, T.L., Gingras, M.K., 2020. Sequence stratigraphy in organic-rich marine mudstone successions using chemostratigraphic datasets. Earth-Science Reviews v. 203, p. 103137.

LaPorte, D. F., Holmden, C., Patterson, W. P., Loxton, J. D., Melchin, M. J., Mitchell, C. E.,

Finney, S. C., and Sheets, H. D., 2009, Local and global perspectives on carbon and nitrogen cycling during the Hirnantian glaciation: Palaeogeography, Palaeoclimatology, Palaeoecology, v. 276, no. 1, p. 182-195.

Li, C., 2019, Middle Ordovician-Llandovery carbon isotope chemostrigraphy in Upper Yangtze Platform, South China [master: University of Science and Technology of China, 105 p.

Li, C., Wu, X., Fan, J., Chen, Q., Li, G., Sun, Z., and Zhang, Y., 2019a, Carbon isotope chemostratigraphy of the Ordovician-Silurian transition interval of the Xike-1 drillcore in Guizhou, China: Geochimica, v. 48, no. 6, p. 533-543.

Li, C., Zhang, J., Li, W., Botting, J., Chen, Q., Fan, J., and Zhang, Y., 2021a, Multiple glacio-eustatic cycles and associated environmental changes through the Hirnantian (Late Ordovician) in South China: Global and Planetary Change, v. 207, p. 103668.

Li, G., Meng, X., Li, S., Feng, M., Xing, C., and Lang, X., 2024, Local depositional and diagenetic conditions control the positive δ34S excursion during the Ordovician-Silurian transition: Evidence from the Wufeng-Longmaxi formations in Sichuan Basin: Palaeogeography, Palaeoclimatology, Palaeoecology, v. 646, p. 112232.

Li, M., Lei, Y., Feng, L., Wang, Z., Belshaw, N. S., Hu, Z., Liu, Y., Zhou, L., Chen, H., and Chai, X., 2018, High-precision Ca isotopic measurement using a large geometry high resolution MC-ICP-MS with a dummy bucket: Journal of Analytical Atomic

Spectrometry, v. 33, no. 10, p. 1707-1719.

Li, N., Li, C., Algeo, T. J., Cheng, M., Jin, C., Zhu, G., Fan, J., and Sun, Z., 2021b, Redox changes in the outer Yangtze Sea (South China) through the Hirnantian Glaciation and their implications for the end-Ordovician biocrisis: Earth-Science Reviews, v. 212, p. 103443.

Li, N., Li, C., Fan, J., Algeo, T. J., Yan, D., Zhu, G., Wu, S., Tang, S., Cheng, M., and Jin, C., 2019b, Sulfate-controlled marine euxinia in the semi-restricted inner Yangtze Sea (South China) during the Ordovician-Silurian transition: Palaeogeography, Palaeoclimatology, Palaeoecology, v. 534, p. 109281.

Li, Y., Zhang, T., Shao, D., and Shen, B., 2019c, New U-Pb zircon age and carbon isotope records from the Lower Silurian Longmaxi Formation on the Yangtze Platform, South China: Implications for stratigraphic correlation and environmental change: Chemical Geology, v. 509, p. 249-260.

Li, Y., Zhang, T., Shen, B., Li, Z., Shao, D., and Lash, G. G., 2021c, Carbon and sulfur isotope variations through the Upper Ordovician and Lower Silurian of South China linked to volcanism: Palaeogeography, Palaeoclimatology, Palaeoecology, v. 567, p. 110285.

Lin, S., Wang, L., Xiao, W., Xing, G., Niu, Z., Zhao, X., Yin, C., Zhang, S., and Liu, H., 2024, The early Paleozoic Wuyi–Yunkai orogeny in South China: a collisional orogeny with a major lag in time between onset of collision and peak metamorphism in subducted continental crust: Geological Society, London, Special Publications, v.

542, no. 1, p. SP542-2023-2026.

Liu, H., 2017, Late Ordovician-Early Silurian productivity and reductive geochemical characteristics of the Lichuan area, Hubei Province, China: Chemical Enterprise Management, no. 15.

Liu, M., Chen, D., Jiang, L., Stockey, R. G., Aseal, D., Zhang, B., Liu, K., Yang, X., Yan, D., and Planavsky, N. J., 2022, Oceanic anoxia and extinction in the latest Ordovician: Earth and Planetary Science Letters, v. 588, p. 117553.

Liu, Y., Li, C., Algeo, T. J., Fan, J., and Peng, P. a., 2016, Global and regional controls on marine redox changes across the Ordovician-Silurian boundary in South China: Palaeogeography, Palaeoclimatology, Palaeoecology, v. 463, p. 180-191.

Lu, Y., Hao, F., Yan, D., and Lu, Y., 2021, Volcanism-induced late Boda warming in the Late Ordovician: Evidence from the Upper Yangtze Platform, South China: Palaeogeography, Palaeoclimatology, Palaeoecology, v. 578, p. 110579.

Lu, Y., Shen, J., Wang, Y., Lu, Y., Algeo, T. J., Jiang, S., Yan, D., and Gou, Q., 2022, Seawater sources of Hg enrichment in Ordovician-Silurian boundary strata, South China: Palaeogeography, Palaeoclimatology, Palaeoecology, v. 601, p. 111156.

Melchin, M. J., and Holmden, C., 2006, Carbon isotope chemostratigraphy in Arctic Canada: Sea-level forcing of carbonate platform weathering and implications for Hirnantian global correlation: Palaeogeography, Palaeoclimatology, Palaeoecology, v. 234, no. 2, p. 186-200.

Men, X., Mou, C., and Ge, X., 2022, Changes in palaeoclimate and palaeoenvironment

in the Upper Yangtze area (South China) during the Ordovician–Silurian transition: Scientific Reports, v. 12, no. 1, p. 13186.

Qiu, Z., Liu, B., Dong, D., Lu, B., Yawar, Z., Chen, Z., and Schieber, J., 2020, Silica diagenesis in the Lower Paleozoic Wufeng and Longmaxi Formations in the Sichuan Basin, South China: Implications for reservoir properties and paleoproductivity: Marine and Petroleum Geology, v. 121, p. 104594.

Qiu, Z., Wei, H., Tian, L., Corso, J. D., Zhang, J., and Zou, C., 2022a, Different controls on the Hg spikes linked the two pulses of the Late Ordovician mass extinction in South China: Scientific Reports, v. 12, no. 1, p. 5195.

Qiu, Z., Zou, C., Mills, B. J. W., Xiong, Y., Tao, H., Lu, B., Liu, H., Xiao, W., and Poulton, S. W., 2022b, A nutrient control on expanded anoxia and global cooling during the Late Ordovician mass extinction: Communications Earth&Environment, v. 3, no. 1, p. 82.

Rong, J., Harper, D. A. T., Huang, B., Li, R., Zhang, X., and Chen, D., 2020, The latest Ordovician Hirnantian brachiopod faunas: New global insights: Earth-Science Reviews, v. 208, p. 103280.

Sánchez-Roda, A., Wignall, P. B., Xiong, Y., and Poulton, S. W., 2024, Redox changes in the Iapetus Ocean during the Late Ordovician extinction crises: Journal of the Geological Society, v. 181, no. 5, p. jgs2023-2195.

Shen, J., Algeo, T. J., Chen, J., Planavsky, N. J., Feng, Q., Yu, J., and Liu, J., 2019, Mercury in marine Ordovician/Silurian boundary sections of South China is

sulfide-hosted and non-volcanic in origin: Earth and Planetary Science Letters, v. 511, p. 130-140.

Shi, X., 2021, A study on the paleoenvironmental changes of Yichang, Hubei in early Silurian [Master: China university of petroleum, 85 p.

Smolarek-Lach, J., Marynowski, L., Trela, W., and Wignall, P. B., 2019, Mercury Spikes Indicate a Volcanic Trigger for the Late Ordovician Mass Extinction Event: An Example from a Deep Shelf of the Peri-Baltic Region: Scientific Reports, v. 9, no. 1, p. 3139.

Stockey, R. G., Cole, D. B., Planavsky, N. J., Loydell, D. K., Frýda, J., and Sperling, E. A., 2020, Persistent global marine euxinia in the early Silurian: Nature Communications, v. 11, no. 1, p. 1804.

Sullivan, N. B., Loydell, D. K., Montgomery, P., Molyneux, S. G., Zalasiewicz, J., Ratcliffe, K. T., Campbell, E., Griffiths, J. D., and Lewis, G., 2018, A record of Late Ordovician to Silurian oceanographic events on the margin of Baltica based on new carbon isotope data, elemental geochemistry, and biostratigraphy from two boreholes in central Poland: Palaeogeography, Palaeoclimatology, Palaeoecology, v. 490, p. 95-106.

Sun, Z., 2018, High-precision integrative stratigraphic research on the Wufeng and Lungmachi formations in South China [doctor: Uiniversity of China Academy of Sciences, 202 p.

Underwood, C. J., Crowley, S. F., Marshall, J. D., and Brenchley, P. J., 1997,

High-Resolution carbon isotope stratigraphy of the basal Silurian Stratotype (Dob's Linn, Scotland) and its global correlation: Journal of the Geological Society, v. 154, no. 4, p. 709-718.

Wang, C., Dong, Z., Fu, X., Chen, Q., Liu, X., Tang, M., and Wang, Z., 2021, Spatiotemporal Evolution and Genesis of the Late Ordovician—Early Silurian Marine Euxinia in Northeastern Upper Yangtze Basin, South China: Frontiers in Earth Science, v. 9.

Wang, Y., Gui, H., Su, S., Zhou, Q., Li, J., and Zhang, Y., 2022, Sedimentary Environment and Paleoclimate Geochemical Characteristics of Shale in the Wufeng and Longmaxi Formations, Northern Yunan-Guizhou Area: Acta Sedimentologica Sinica, v. 40, no. 3, p. 653-666.

Wang, Y., Rong, J., Zhan, R., Huang, B., Wu, R., and Wang, G., 2013, On the Ordovician-Silurian boundary strata in southwestern Hubei, and the Yichang uplift: Journal of Stratigraphy, v. 37, no. 3, p. 265-274.

Xi, Z., Tang, S., Lash, G. G., Zhang, B., and Lin, D., 2021, Geochemical characteristics of organic carbon and pyrite sulfur in Ordovician-Silurian transition shales in the Yangtze Platform, South China: Implications for the depositional environment: Palaeogeography, Palaeoclimatology, Palaeoecology, v. 563, p. 110173.

Xiao, B., Xiong, L., Zhao, Z., and Fu, X., 2022, Sedimentary tectonic pattern of Wufeng and Longmaxi Formations in the northern margin of Sichuan Basin, South China: International Geology Review, v. 64, no. 15, p. 2166-2185.

585 Xiao, Q., Zhang, T., Zhang, X., Li, H., Yong, J., Liu, Y., and Li, X., 2021, Organic matter
586 enrichment in Wufeng Formation-Longmaxi Formation in southern Sichuan: based
587 on cyclostratigraphy: Marine Origin Petroleum Geology, v. 26, no. 2, p. 105-112.
588 Yan, D., Chen, D., Wang, Q., Wang, J., and Wang, Z., 2009, Carbon and sulfur isotopic
589 anomalies across the Ordovician–Silurian boundary on the Yangtze Platform,
590 South China: Palaeogeography, Palaeoclimatology, Palaeoecology, v. 274, no. 1,
591 p. 32-39.
592 Yan, D., Chen, D., Wang, Z., Li, J., Yang, X., and Zhang, B., 2019, Climatic and oceanic
593 controlled deposition of Late Ordovician-Early Silurian black shales on the North
594 Yangtze platform, South China: Marine and Petroleum Geology, v. 110, p.
595 112-121.
596 Young, S. A., Benayoun, E., Kozik, N. P., Hints, O., Martma, T., Bergström, S. M., and
597 Owens, J. D., 2020, Marine redox variability from Baltica during extinction events
598 in the latest Ordovician–early Silurian: Palaeogeography, Palaeoclimatology,
599 Palaeoecology, v. 554, p. 109792.
600 Young, S. A., Saltzman, M. R., Ausich, W. I., Desrochers, A., and Kaljo, D., 2010, Did
601 changes in atmospheric CO2 coincide with latest Ordovician glacial–interglacial
602 cycles?: Palaeogeography, Palaeoclimatology, Palaeoecology, v. 296, no. 3, p.
603 376-388.
604 Zhan, R., and Jin, J., 2007, Ordovician-Early Silurian(Llandovery) Stratigraphy and
605 Palaeontology of the Upper Yangtze Platform, South China.

606 Zhan, R., Jin, J., Liu, J., Corcoran, P., Luan, X., and Wei, X., 2016, Meganodular limestone
607 of the Pagoda Formation: A time-specific carbonate facies in the Upper
608 Ordovician of South China: Palaeogeography, Palaeoclimatology, Palaeoecology,
609 v. 448, p. 349-362.
610 Zhang, J., Lyons, T. W., Li, C., Fang, X., Chen, Q., Botting, J., and Zhang, Y., 2022, What
611 triggered the Late Ordovician mass extinction (LOME)? Perspectives from
612 geobiology and biogeochemical modeling: Global and Planetary Change, v. 216,
613 p. 103917.
614 Zhang, L., Fan, J., and Chen, Q., 2016, Geographic distribution and palaeogeographic
615 reconstruction of the Upper Ordovician Kuanyinchiao Bed in South China: Chinese
616 Science Bulletin, v. 61, no. 18, p. 2053-2063.
617 Zhang, L., Fan, J., Wang, B., Zhang, Y., Liu, J., Huang, H., and Chen, Q., 2023,
618 Quantitative paleogeographical reconstructions and basin evolution of South
619 China during the Ordovician: Earth-Science Reviews, v. 241, p. 104400.
620 Zhang, T., Shen, Y., Zhan, R., Shen, S., and Chen, X., 2009, Large perturbations of the
621 carbon and sulfur cycle associated with the LateOrdovician mass extinction in
622 South China: Geology, v. 37, no. 4, p. 299-302.
623 Zhang, X., Zhang, T., Zhao, X., Zhu, H., Mihai, E. P., Chen, L., Yong, J., Xiao, Q., and Li, H.,
624 2021, Effects of astronomical orbital cycle and volcanic activity on organic
625 carbon accumulation during Late Ordovician–Early Silurian in the Upper Yangtze
626 area, South China: Petroleum Exploration and Development, v. 48, no. 4, p.

850-863.

Zhong, Y., Wu, H., Fan, J., Fang, Q., Shi, M., Zhang, S., Yang, T., Li, H., and Cao, L., 2020, Late Ordovician obliquity-forced glacio-eustasy recorded in the Yangtze Block, South China: Palaeogeography, Palaeoclimatology, Palaeoecology, v. 540, p. 109520.

Zhou, Y., Ding, J., Yu, Q., Wang, J., Men, Y., Xiong, G., Xiong, X., and Deng, Q., 2017, Sedimentary and Organic Carbon Isotopic Characteristics of the Kuanyinchiao Member in Northeastern Chongqing and Its Regional Correlation: Acta Geologica Sinica, v. 91, no. 5, p. 1097-1107.

Zou, C., Qiu, Z., Poulton, S. W., Dong, D., Wang, H., Chen, D., Lu, B., Shi, Z., and Tao, H., 2018, Ocean euxinia and climate change “double whammy” drove the Late Ordovician mass extinction: Geology, v. 46, no. 6, p. 535-538.